40th Fluid Dynamics Conference and Exhibit
28 June - 1 July 2010, Chicago, Illinois

AIAA 2010-4863

Computation of the Flow of a Dual-Stream Jet with External Solid and Perforated Wedge Deflectors for Noise Reduction

Juntao Xiong*, Feng Liu† and Dimitri Papamoschou‡

University of California Irvine, Irvine, CA, 92697, USA

We present a methodology for the computation of flow fields involving complex perforated surfaces in propulsion applications. Of particular interest is the treatment of perforated flaps used as wedge-shaped fan flow deflectors for reducing jet noise of a supersonic turbofan engine. A three-dimensional Reynolds-Averaged Navier-Stokes solver is used to compute the flow field of the external jet plume with solid and perforated deflector flaps, the latter with 50% porosity. Flow computation for perforated flaps presents a particular challenge and is handled by use of a localized body force model in the momentum equation. The study is conducted at two operating conditions: a cold condition at which mean velocity surveys were conducted and against which the computational code is validated; and a hot condition that corresponds to the takeoff engine cycle. The code predictions replicate adequately the mean velocity fields of the cold experimental flows. The code is then extended to the conditions of the actual engine cycle to study the impacts of the deflectors on the turbulent kinetic energy (TKE) distributions in the jet plume and on the aerodynamic performance of the nozzle. Consistent with findings of past studies, the solid flaps decrease the TKE on the underside of the jet and increase it at the top of the jet. The perforated flaps mitigate the TKE increase on the top of the jet, thus reducing the potential of excess noise from that region. The thrust loss of the perforated flaps is approximately one half that of the solid flaps.

Nomenclature

A	=	area
a	=	speed of sound
c	=	wedge/flap "chord" length
C_p	=	pressure coefficient
D_f	=	nozzle fan diameter
E	=	total internal energy
F_c	=	inviscid convective flux
F_d	=	inviscid diffusive flux
k	=	turbulent kinetic energy
k_{max}	=	maximum k along a given radial direction
k_{peak}	=	maximum k on a given azimuthal plane ϕ=ϕ_0
M	=	Mach number
NPR	=	nozzle pressure ratio
p	=	static pressure
r	=	radial direction
U	=	nozzle exit or ambient velocity
u, v, w	=	velocity components
W	=	conservative variable vector

*Post-doctoral Researcher, Department of Mechanical Aerospace Engineering, Member AIAA
†Professor, Department of Mechanical and Aerospace Engineering, Associate Fellow AIAA
‡Professor, Department of Mechanical and Aerospace Engineering, Fellow AIAA

x, y, z	=	Cartesian coordinates
β	=	porosity
μ_L	=	molecular viscosity
μ_T	=	turbulent viscosity
ρ	=	density
τ	=	stress tensor
ϕ	=	azimuth angle from downward vertical
Ω	=	vorticity
ω	=	specific dissipation rate

Subscript

a	=	ambient
p	=	primary exhaust
s	=	secondary exhaust

I. Introduction

This study is motivated by the advent of wedge-shaped fan flow deflectors for reduction of jet noise from separate-flow turbofan engines. The role of the deflectors is to direct some of the fan stream underneath the core stream, thus reducing velocity gradients and turbulence production on the underside of the jet. Figure 1 depicts a generic setup for the low-bypass cycle considered in this study. The deflectors belong to the general class of "offset stream technologies", including internal vanes, wedges, and eccentric nozzles, that have been shown to reduce downward noise in small-scale and large-scale tests.[1,2] Experiments and computations have revealed that the deflectors reduce the downward turbulent kinetic energy (TKE) but can also introduce a localized increase in the upward TKE.[3–6] Recent work has shown a correlation between the reduction in downward TKE and the reduction in downward peak overall sound pressure level.[7]

The wedge-shaped deflector is an intriguing device with strong potential benefits but requiring great care in its design. One main benefit is that the wedge can be shaped into deployable flaps that confine aerodynamic penalties only to the noise-critical segments of flight (typically takeoff). On the other hand, the wedge creates a "dead-flow" region in its wake that exposes the core stream directly to the ambient flow. This increases local velocity gradients which can lead to excess noise generation. Experiments using a phased microphone array[8] located this excess noise near the base of the wedge (or solid flaps). The deflector self-noise influences mainly the large polar angles from the jet axis can be strong enough to reduce and even reverse the perceived-noise benefits stemming from the downward reduction in TKE. A proposed solution is the use of porous flaps that allow some flow at the wedge base, thus mitigating the excess gradients. Subscale experiments at U.C. Irvine have shown consistent noise benefits of porous flaps over solid flaps or wedges, for subsonic and supersonic engine cycles, including integration with a pylon.[8,9] Porosities of about 50% are deemed optimal.

In recent years Reynolds Averaged Navier Stokes (RANS) solvers, in combination with Acoustic Analogy models, are showing promise as engineering tools for predicting noise and its reduction.[10,11] Such an approach, with very simplified acoustic analogy treatment, has already demonstrated benefits in our efforts to optimize internal-vane fan flow deflectors for a supersonic turbofan cycle and nozzle configuration.[7] The computation of wedge-shaped flap deflectors poses significant challenges, particularly for porous flaps. It is not computationally feasible to grid the numerous perforations of a porous flap. We seek alternative approaches that involve a suitable boundary condition, calibrated by experiments on canonical perforated plates.

In this article, a computational model is developed as a tool to predict the effect of wedge-shaped deflectors on the mean-velocity and TKE distributions in the plume of a dual-stream jet replicating the conditions of a supersonic turbofan engine with bypass ratio 2.7. The deflectors comprise a solid wedge, solid flaps, and porous flaps with porosity $\beta = 0.5$ The investigation starts with validation of the computational mean-velocity results against experimental data acquired at cold jet conditions. Once validated, the computation is then extended to hot conditions corresponding to takeoff engine cycle. The TKE fields for the deflector configurations are then computed at the hot cycle point. In addition, we examine the aerodynanics of the deflectors and the related thrust loss.

II. Computational Approach

II.A. Numerical Code

The computational fluid dynamics code used here is known as PARCAE and it solves the unsteady three-dimensional Reynolds-averaged Navier-Stokes (RANS) equations on structured multiblock grids using a cell-centered finite-volume method with artificial dissipation as proposed by Jameson et al.[12] Information exchange for flow computation on multiblock grids using multiple CPUs is implemented through the MPI (Message Passing Interface) protocol. The RANS equations are solved using the eddy viscosity type turbulence models. The code contains the Baldwin-Lomax algebraic model[13] , Spalart-Allmaras one-equation model,[14] k-ω two-equation model,[15] and Menter SST k-ω model.[16] In this study, only the steady-state solution is obtained because we are interested in the time-averaged features of the flow. All computations presented in this work are performed using the SST model. The SST turbulence model combines the advantages of the k-ω and k-ϵ turbulence models for both wall boundary layer and free-stream flows. The main elements of the code are summarized below.

The governing equations for the unsteady compressible turbulent flow with SST turbulence model are expressed as follows:

$$\frac{\partial}{\partial t}\int_{\Omega} \mathbf{W}\, d\Omega + \oint_{\partial\Omega} (\mathbf{F}_c - \mathbf{F}_d)\, dS = \int_{\Omega} \mathbf{S}\, d\Omega \tag{1}$$

The vector $\mathbf{W}$ contains the conservative variables

$$\mathbf{W} = \left\{ \ \rho, \rho u, \rho v, \rho w, \rho E, \rho k, \rho\omega \ \right\}^{\mathrm{T}} \tag{2}$$

The fluxes consist of the inviscid convective fluxes $\mathbf{F}_c$ and the diffusive fluxes $\mathbf{F}_d$. For the convective fluxes we include the pressure term

$$\mathbf{F}_c = \left\{ \begin{array}{ccc} \rho u & \rho v & \rho w \\ \rho uu + p & \rho uv & \rho uw \\ \rho vu & \rho vv + p & \rho vw \\ \rho wu & \rho wv & \rho ww + p \\ \rho E u + pu & \rho E v + pv & \rho E w + pw \\ \rho k u & \rho k v & \rho k w \\ \rho\omega u & \rho\omega v & \rho\omega w \end{array} \right\} \tag{3}$$

For the diffusive fluxes we have

$$\mathbf{F}_d = \left\{ \begin{array}{ccc} 0 & 0 & 0 \\ \tau_{xx} & \tau_{xy} & \tau_{xz} \\ \tau_{yx} & \tau_{yy} & \tau_{yz} \\ \tau_{zx} & \tau_{zy} & \tau_{zz} \\ \theta_x & \theta_y & \theta_z \\ \mu_k^* \frac{\partial k}{\partial x} & \mu_k^* \frac{\partial k}{\partial y} & \mu_k^* \frac{\partial k}{\partial z} \\ \mu_\omega^* \frac{\partial \omega}{\partial x} & \mu_\omega^* \frac{\partial \omega}{\partial y} & \mu_\omega^* \frac{\partial \omega}{\partial z} \end{array} \right\} \tag{4}$$

where

$$\begin{aligned} \mu_k^* &= \mu_L + \sigma_k \mu_T \\ \mu_\omega^* &= \mu_L + \sigma_\omega \mu_T \\ \mu_T &= \frac{\rho a_1 k}{max(a_1\omega; \omega F_2)} \end{aligned}$$

and

$$\theta_x = u\tau_{xx} + v\tau_{xy} + w\tau_{xz} + \mu^* \frac{\partial k}{\partial x} - (\frac{\mu_L}{\mathrm{Pr}_L} + \frac{\mu_T}{\mathrm{Pr}_T})\frac{\partial T}{\partial x}$$

$$\theta_y = u\tau_{xy} + v\tau_{yy} + w\tau_{zy} + \mu^* \frac{\partial k}{\partial y} - (\frac{\mu_L}{\mathrm{Pr}_L} + \frac{\mu_T}{\mathrm{Pr}_T})\frac{\partial T}{\partial y}$$

$$\theta_z = u\tau_{xz} + v\tau_{yz} + w\tau_{zz} + \mu^* \frac{\partial k}{\partial z} - (\frac{\mu_L}{\mathrm{Pr}_L} + \frac{\mu_T}{\mathrm{Pr}_T})\frac{\partial T}{\partial z}$$
$$\mu^* \;=\; \mu_L + \sigma^* \mu_T$$

with τ being the stress tensor. The source term is

$$\mathbf{S} = \left\{ \begin{array}{c} 0 \\ 0 \\ 0 \\ 0 \\ 0 \\ \tau_{ij}\frac{\partial u_i}{\partial x_j} - \eta^* \rho \omega k \\ \frac{\eta'}{\nu_t}\tau_{ij}\frac{\partial u_i}{\partial x_j} - \eta\rho\omega^2 + 2\rho(1-F_1)\frac{1}{\omega}\frac{\partial k}{\partial x_j}\frac{\partial \omega}{\partial x_j} \end{array} \right\} \tag{5}$$

In the above equations, F_1 and F_2 are blending functions. The parameters σ_k, σ_ω, η, η^*, and η' are closure coefficients for the turbulence model. The equations are discretized in space by a structured hexahedral grid using a cell-centered finite-volume method. Since within the code each block is considered as a single entity, only flow and turbulence quantities at the block boundaries need to be exchanged. The governing equations are solved explicitly in a coupled manner through a five stage Runge-Kutta scheme towards the steady state with local-time stepping, residual smoothing, and multigrid for convergence acceleration. Unlike previous computational studies of fan flow deflection,[5] a low-speed preconditioner[17] is employed to simulate low ambient Mach number of the nozzle and jet plume flows. Further details of the numerical method can be found in Refs.[7,18]

II.B. Modeling of Flaps

In order to model the effect of solid or perforated flaps, a body force term $\vec{F_b}$ is implemented in the momentum equation and applied locally at the media cells defining the flap:

$$\frac{\partial \rho \vec{u}}{\partial t} + \bigtriangledown \cdot (\rho \vec{u}\vec{u}) = -\bigtriangledown p + \bigtriangledown \cdot \vec{\tau} - \vec{F_b} \tag{6}$$

The body force generates a momentum sink that results in a pressure drop across the media. The pressure drop across a perforated plate can be represented by the sum of a viscous loss term proportional to the permeation velocity and an inertial loss term proportional to the square of the permeation velocity.[19] The Reynolds numbers of the flowfield considered here is sufficiently high to justify neglecting the viscous term. The locally-applied body force can then be written as

$$\vec{F_b} = \frac{1}{2} C \rho |\vec{u}| \vec{u} \tag{7}$$

where C is a dimensional inertial resistance coefficient.

The model of Eqs. 6 and 7 is calibrated against measurements of drag coefficient for a perforated plate inclined normal to a freestream.[20] The relationship between porosity and drag coefficient is shown in Fig.2 for the referenced experiment and the body-force model. The overall trend in the relationship between the two parameters is reproduced well by the body force model. This provides a preliminary calibration for applying this model to solid and porous fan flow deflector flaps.

II.C. Computational Model and Grid

The coordinates of the dual-stream nozzle are plotted in Fig. 3. Operated at the takeoff cycle point, the bypass ratio is BPR=2.7. The dimensions of the nozzle correspond to the subscale model used in aeroacoustic tests at U.C. Irvine.[21] The fan diameter is D_f=28.1 mm and and the fan exit height is 1.8 mm. Reshaping of the jet plume is achieved by using external wedge-shaped deflectors. This study considers deflectors in the forms of a solid wedge, solid flaps, and perforated flaps. All the deflectors have a side length of 10 mm, height of 4 mm, and half angle of 20°. They are positioned 4 mm downstream of the fan exit plane.

Multiblock grids are generated for each configuration. Because the arrangements are symmetric to the meridional plane, only one half (180°) of the nozzle was modeled to reduce computational cost. In order to simulate the jet flow, the grid was extended $3.8D_f$ radially outward from the nozzle centerline and over $20D_f$ downstream of the nozzle. A patch-connection interpolation technique is used to transfer flow variable information between non-matching connection surfaces. Figure 4 shows the grids for the baseline nozzle and for the nozzle with solid wedge deflector.

II.D. Flow and Boundary Conditions

The study is conducted two operating conditions: a cold condition at which mean velocity surveys were conducted and against which the computational code is validated; and a hot condition that corresponds to the takeoff engine cycle. The nozzle exit conditions for the two set points are listed in Table 1. While the experiments were static, the computations are performed with a small forward ambient velocity of 17 m/s (M_a=0.05) for reasons of numerical stability. For the two streams of the nozzle, uniform total pressure, uniform total temperature, and zero flow angle are specified at the inlet surface corresponding to a perfectly expanded exit Mach number. For the ambient region surrounding the nozzle flow, a characteristic boundary condition is defined, and the downstream static pressure is set to the ambient pressure. The adiabatic no-slip boundary condition is specified on all nozzle and vane solid walls. The jet Reynolds number, based on the exit diameter of the fan nozzle, for the hot and cold conditions are 0.92×10^6 and 0.47×10^6, respectively. For the cold case the total temperature of both streams is set to the ambient value. Nozzle thrust is determined by integration of momentum and pressure over a control volume that includes the entire nozzle.

III. Results and Discussion

The computations are first validated with experimental measurements of the mean velocity field at the cold condition. Then the code is extended to the hot condition to investigate the TKE effects of different external wedge-shape deflector configurations, flow field around the wedges, and the impact on nozzle aerodynamic performance.

III.A. Validation Against Mean Flow Measurements

The computational code is validated by comparing the computed axial velocity of the jet to experimental measurements, performed at cold conditions. We examine contour plots of the mean velocity on the symmetry plane and various cross-sectional planes as well as velocity line plots at different axial positions. The results of the baseline nozzle are shown in Fig. 5. Contours on the symmetry plane indicate very similar potential core lengths. The velocity profiles match the experimental ones well except at the centerline close to the nozzle exit where the computational result shows a deeper wake deficit behind the nozzle plug. This difference, however, becomes small as the flow moves downstream. Note a slight difference in the ambient conditions caused by the small forward velocity (17 m/s) needed in the computations.

In the perforated flap case of Fig. 6, the computed and experimental cross-sectional velocity contours show deformation of the flow into a “pear-shaped” profile, with notable thickening of the secondary layer beneath the primary jet, which contributes to the reduction of downward-emitted noise. Again the computed velocity profiles match reasonably well those of the experiment. The close agreement between the computed results with experiments lends confidence for the application of the computational code to evaluate the effects of TKE and the aerodynamic performance at the hot set point.

III.B. Mean Velocity for Hot Condition

Figures 7-8 present velocity results for the baseline nozzle and the nozzle with porous flaps at the hot set point. For the baseline nozzle, contrasting with the cold case of Fig. 5, we note a moderate reduction on the length of the potential core. This is expected due to the enhanced growth rate of the lighter jet. The porous flaps cause deformations similar to those seen in the cold case of Fig. 6.

III.C. Turbulent Kinetic Energy

We examine distributions of the normalized turbulent kinetic energy $k^* = k/U_p^2$ on the symmetry plane and three cross-sectional planes for the hot set point. Figures 9 - 12 present results for the baseline, solid-wedge, solid-flap, and porous-flap nozzles. Table 2 summarizes the peak values of TKE in the downward ($\phi = 0°$), sideline ($\phi = 60°$), and upward ($\phi = 180°$) directions. The figures and table show that fan flow deflection reduces the turbulent kinetic energy in both the downward and sideline directions when compared to the baseline case. The solid deflectors produce significant downward TKE reductions but with a substantial increase, of about 50%, at the top of the jet. Use of porous flaps mitigates this increase to only 34%. Thus the porous flaps provide the desired effect of preventing strong gradients and TKE production at the top of the jet. There are no significant differences in the TKE fields produced by the two solid deflectors.

Further insight into the TKE redistributions is gained by plotting the maximum value of turbulence kinetic energy, k^*_{max}, in a given azimuthal direction ϕ, as a function of x and ϕ. Figure 13(a) displays contour maps of $k^*_{max}(x, \phi)$ for the porous flap case. The low levels of turbulent kinetic energy at the bottom of the jet ($\phi = 0°$) and large values at the top of the jet ($\phi = 180°$) are evident. At the bottom of the jet, k^*_{max} peaks near $x/D_f = 4.0$, which is slightly downstream of the end of the potential core. With increasing azimuth angle, the location of peak k^*_{max} shifts toward the nozzle exit. Figure 13(b) presents a differential map of k^*_{max} whereby the values of the baseline have been subtracted from the values of the wedge case. This map highlights the changes in the TKE field due to the fan flow deflection. Broad reductions are seen in the downward and sideline directions, with a highly localized peak near the top of the nozzle ($\phi \approx 180°$) in the vicinity of the base of the deflector.

III.D. Aerodynamics

The wedge-shaped fan flow deflectors create complex flow patterns seen in the Mach number contours and streamlines of Fig. 14. The computed streamline pattern over the side of wedge is in good agreement with past experimental surface flow visualizations.[22] A stagnation point occurs on the apex of the wedge at the cowl surface where the wedge is mounted. This is the only front stagnation point in the wedge flow. As we move away from the cowl, and staying in the vicinity of the apex, the streamlines are deflected progressively upward, with the streamline of the free surface being deflected the most. The upwash of the free surface is a consequence of the compression occurring over the side surface of the wedge. There are no remarkable differences between the flow fields of the solid wedge and solid flaps. In contrast, the flow field of the porous flaps shows a more benign upwash, with flow at the base of the flaps being obvious. The small forward velocity of the ambient stream creates a large separation vortex over the wedge; however its strength is much smaller than the strength of phenomena related to the fan flow deflection by the wedge.

The three-dimensional nature of the flow is also evident in the distributions of pressure coefficient over the surface of the solid wedge and porous flaps, shown respectively in Figs. 15 and 16. In these figures the pressure distribution is plotted on different normalized heights y/h over the cowl surface, with h the wedge/flap height. The largest compression occurs right on the apex, which acts as a singularity. The compression relaxes very rapidly to moderate levels over the side surface of the wedge/flap, with a weakly negative pressure at the base. As we move from the bottom to the top of the wedge, the compression becomes progressively weaker and the pressure reaches the ambient value at the top of the wedge. Comparing the porous flap to the solid wedge, we note that both deflectors develop a compression over their surface, which forces the flow away from the symmetry plane at the top of the jet. The porous flap develops less suction over the base and has slightly weaker compression on its side. The near-zero base pressure coefficient for the porous flap results in a much smaller drag as will be shown next.

The thrust losses are listed in Table 3. For the solid configurations, the wedge results in a thrust loss of 1.2% and the flaps result in a thrust loss of 1.03%. In terms of an equivalent 2D drag coefficient for the wedge (scaled by the base width), these losses correspond to $C_d \approx 0.25$. This should be contrasted with $C_d \approx 1.0$ for a wedge cylinder of the same half-angle.[23] The reduced drag of the fan flow deflector wedge arises from the exposure of its base to the ambient, resulting in a very weak base suction. Introducing perforations with porosity of 50% reduces the thrust loss by about half to 0.53%. A thrust loss on the order of 0.5% would affect minimally takeoff performance. Further, with use of deployable flaps, the performance penalty over the entire mission of the aircraft would be negligible.

IV. Conclusion

This study introduces a methodology for the computation of complex three-dimensional flow fields generated by thin surfaces that can be porous. The specific motivation is the wedge-shape fan flow deflectors used for noise reduction of turbofan engines. An efficient configuration of these devices is a deployable flap arrangement. Porous flaps mitigate localized strong turbulence production that could create excess noise. However, their computational treatment presents severe challenges that this study tries to address.

A three-dimensional Reynolds-Averaged Navier-Stokes solver is used to compute the flow field of the external jet plume with solid and perforated deflector flaps, the latter with 50% porosity. The thin flaps are handled by use of a localized body force model in the momentum equation. The study is conducted two operating conditions: a cold condition at which mean velocity surveys were conducted and against which the computational code was validated; and a hot condition that corresponds to the takeoff engine cycle. The code predictions replicate adequately the mean velocity fields of the cold experimental flows. The code is then extended to the conditions of the actual engine cycle to study the impacts of the deflectors on the turbulent kinetic energy (TKE) distributions in the jet plume.

Consistent with findings of past studies, the solid flaps decrease the TKE at on the underside of the jet and increase it at the top of the jet. The perforated flaps mitigate the TKE increase on the top of the jet, thus reducing a potentially adverse source of noise. The thrust loss of the perforated flaps with approximately 50% of that of the solid flaps. The reduced drag of the perforated flaps is attributed to a near-zero base pressure in their wake.

Acknowledgements

The support by NASA Cooperative Agreement NNX07AC62A, monitored by Dr. K.B.M.Q. Zaman, is gratefully acknowledged.

References

[1] Papamoschou, D., "Fan Flow Deflection in Simulated Turbofan Exhaust," *AIAA Journal*, Vol. 44, No. 12, 2006, pp. 3088–3097.

[2] Brown, C., Bridges, J., and Henderson, B., "Offset Stream Technologies Test - Summary of Results," AIAA 2007-3664, May 2007.

[3] Shupe, R. S., Zaman, K. B. M. Q., and Papamoschou, D., "Effects of Wedge-Shape Deflectors on Flow Fields of Dual-Stream Jets," AIAA 2007-3659, May 2007.

[4] Shupe, R. and DeBonis, J., "Flow Field of a Dual-Stream Jet with External Wedge-Shaped Deflector," AIAA 2008-0042, January 2008.

[5] Dippold, V., Foster, L., and Wiese, M., "Computational Analyses of Offset Stream Nozzles for Noise Reduction," *Journal of Propulsion and Power*, Vol. 25, No. 1, 2009, pp. 204–217.

[6] DeBonis, J., "RANS Analyses of Turbofan Nozzles With Internal Wedge Deflectors for Noise Reduction," *Journal of Fluids Engineering*, Vol. 131, Apr. 2009.

[7] Xiong, J., Nielsen, P., Liu, F., and Papamoschou, D., "Computation of High-Speed Coaxial Jets with Fan Flow Deflection," to appear in the AIAA Journal.

[8] Papamoschou, D., "Pylon Based Jet Noise Suppressors," *AIAA Journal*, Vol. 47, No. 6, 2009, pp. 1408–1420.

[9] Nielsen, P. and Papamoschou, D., "Mean Flow-Acoustic Correlations for Dual-Stream Asymmetric Jets," AIAA 2009-0853, January 2009.

[10] Morris, P. J. and Farassat, F., "Acoustic Analogy and Alternative Theories for Jet Noise Prediction," *AIAA Journal*, Vol. 40, No. 4, 2002, pp. 671–680.

[11] Birch, S. F., Lyubimov, D. A., Maslov, V. P., Secundov, A. N., and Yakubosky, Y., "A RANS based Jet Noise Prediction Procedure," AIAA 2007-3727, May 2007.

[12] Jameson, A., Schmift, W., and Turkel, E., "Numerical Solutions of the Euler Equations by Finite Volume Methods Using Runge-Kutta Time Stepping Schemes," AIAA 1981-1259, January 1981.

[13] Baldwin, B. S. and Lomax, H., "Thin-Layer Approximation and Algebraic Model for Separation Flows," AIAA 1978-0257, January 1978.

[14] Spalart, P. R. and Allmaras, S. R., "A One-Equation Turbulence Model for Aerodynamic Flows," AIAA 1992-0439, January 1992.

[15] Wilcox, D., "Reassessment of the Scale Determining Equation for Advanced Turbulence Models," *AIAA Journal*, Vol. 26, No. 11, 1988, pp. 1299–1310.

[16] Menter, F., "Two-Equation Eddy-Viscosity Turbulence Models for Engineering Applications," *AIAA Journal*, Vol. 32, No. 8, 1994, pp. 1598–1605.

[17] Turkel, E., "A Review of Preconditioning Methods for Fluid Dynamics," *Applied Numerical Mathematics*, Vol. 12, No. 1, 1993, pp. 257–284.

[18] Xiong, J., Nielsen, P., Liu, F., and Papamoschou, D., "Computational Validation of Fan Flow Deflection for Supersonic Turbofan Engines," AIAA 2009-3254, January 2009.

[19] Sozer, E., Shyy, W., and Thakur, S., "Multi-Scale Porous Media Modeling for Liquid Rocket Injector Applications," AIAA 2006-5044, July 2006.

[20]Castro, I. P., "Wake Characteristics of Two-Dimensional Perforated Plates Normal to an Air-Stream," *Journal of Fluid Mechanics*, Vol. 46, No. 3, 1971, pp. 599–609.

[21]Papamoschou, D. and Nielsen, P., "Fan Flow Deflection for Supersonic Turbofan Engines," AIAA 2008-0039, January 2008.

[22]Papamoschou, D., Vu, A., and Johnson, A., "Aerodynamics of Wedge-Shaped Deflectors for Jet Noise Reduction," AIAA 2006-3655, June 2006.

[23]Hoerner, S., "Fluid-Dynamic Drag," Hoerner Fluid Dynamics, Brick Town, N. J., USA, 1965.

Table 1 Exhaust Conditions

	Hot(cycle point)	Cold
U_p (m/s)	600	319
M_p	1.03	1.03
NPR_p	2.00	1.96
U_s (m/s)	400	213
M_s	1.15	0.65
NPR_s	2.25	1.33
A_s/A_p	1.4	1.40
U_s/U_p	0.67	0.67

Table 2 Peak Value of Turbulent Kinetic Energy

Configuration	$k^*{}_{peak}$,lower	$k^*{}_{peak}$,sideline	$k^*{}_{peak}$,upper
Base	0.0212	0.0212	0.0212
Solid wedge	0.0180	0.0177	0.0324
Solid flaps ($\beta = 0.0$)	0.0179	0.0182	0.0316
Porous flaps ($\beta = 0.5$)	0.0199	0.0200	0.0285

Table 3 Aerodynamic Performance

Configuration	Thrust loss
Solid wedge	1.20%
Solid flaps ($\beta = 0.0$)	1.03%
Porous flaps ($\beta = 0.5$)	0.53%

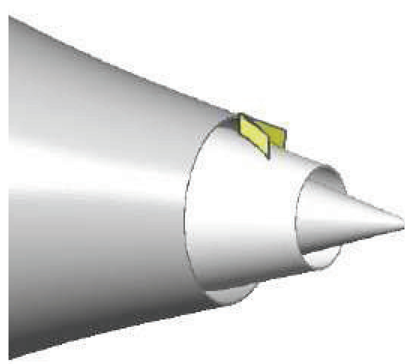

Figure 1. Illustration of fan flow deflector in the form of wedge-shaped flaps.

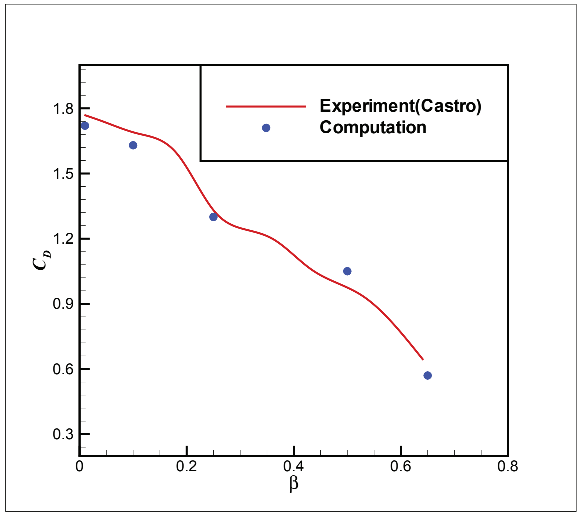

Figure 2. Drag coefficient versus porosity for a perforated plate normal to the flow.

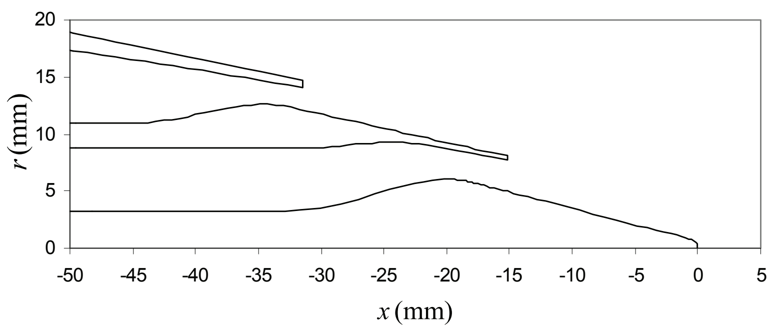

Figure 3. Coordinates of the bypass ratio BPR = 2.7 nozzle.

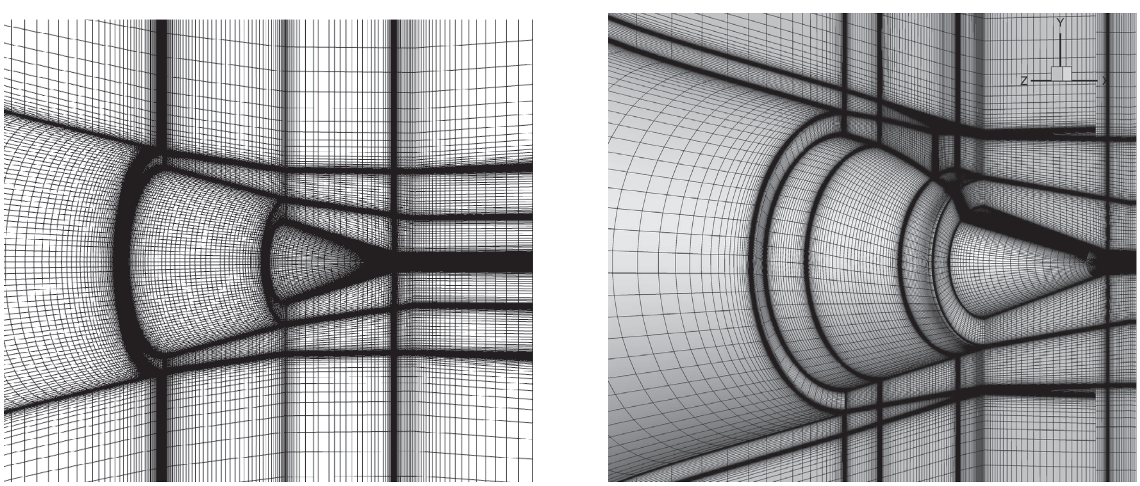

(a) Baseline nozzle

(b) Solid wedge nozzle

Figure 4. Computational grids.

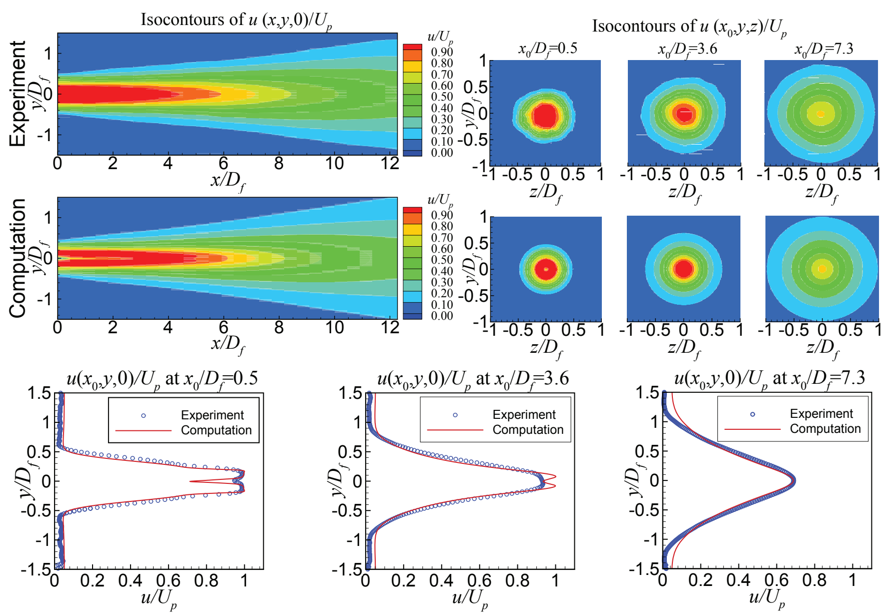

Figure 5. Comparison of computational and experimental velocity fields for the baseline nozzle.

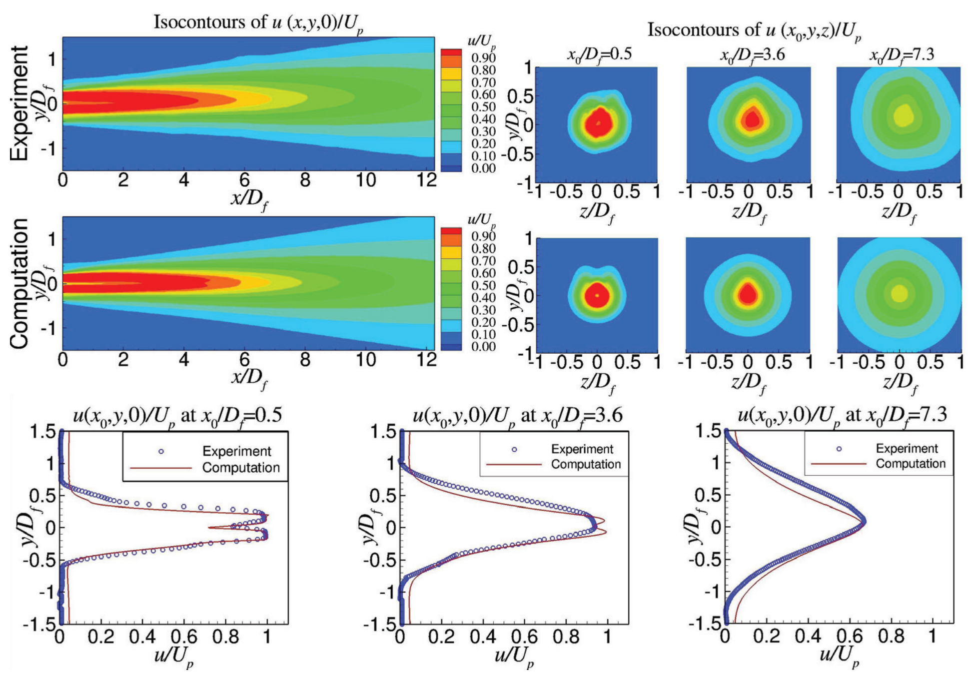

Figure 6. Comparison of computational and experimental velocity fields for the porous flaps ($\beta = 0.5$).

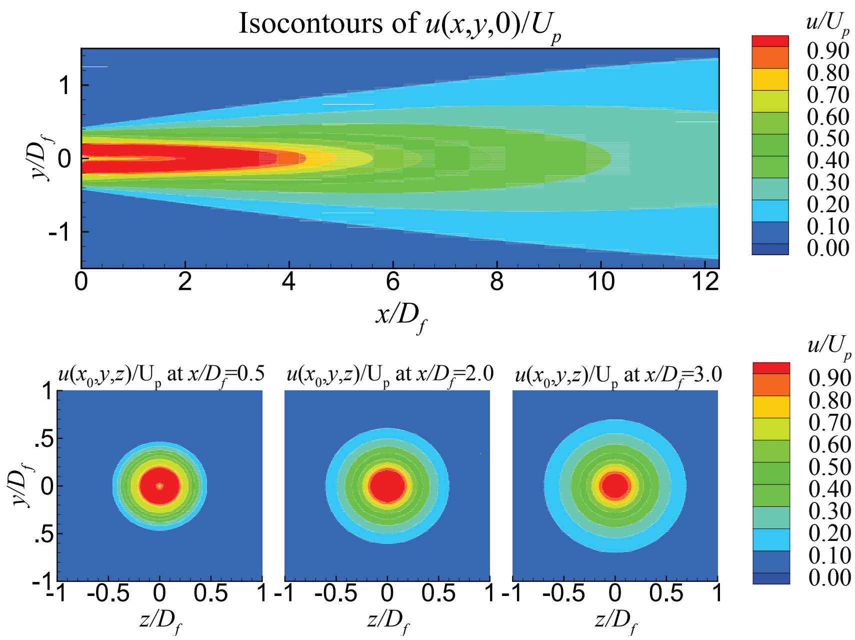

Figure 7. Computational velocity field for the baseline nozzle at hot condition.

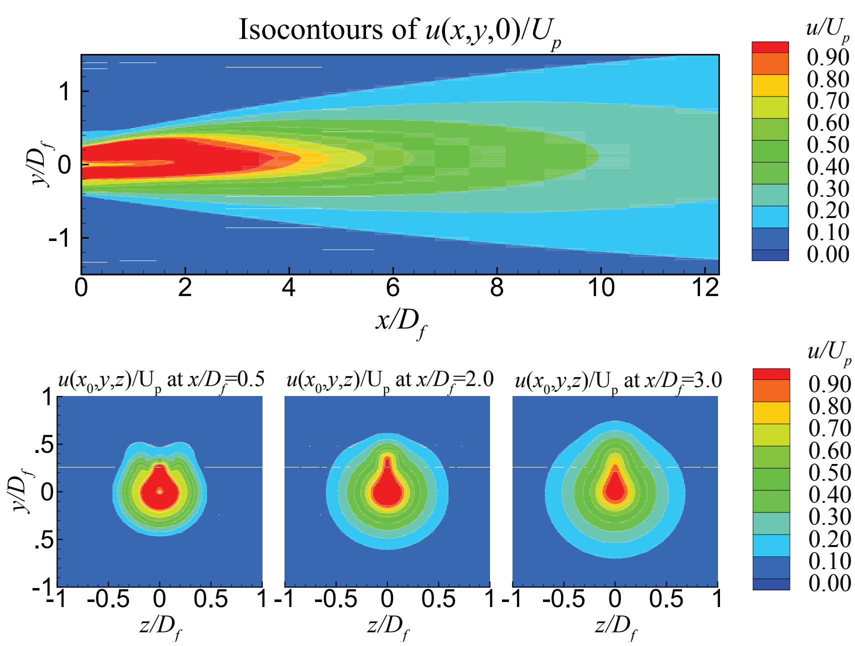

Figure 8. Computational velocity field for the porous flaps ($\beta = 0.5$) at hot condition.

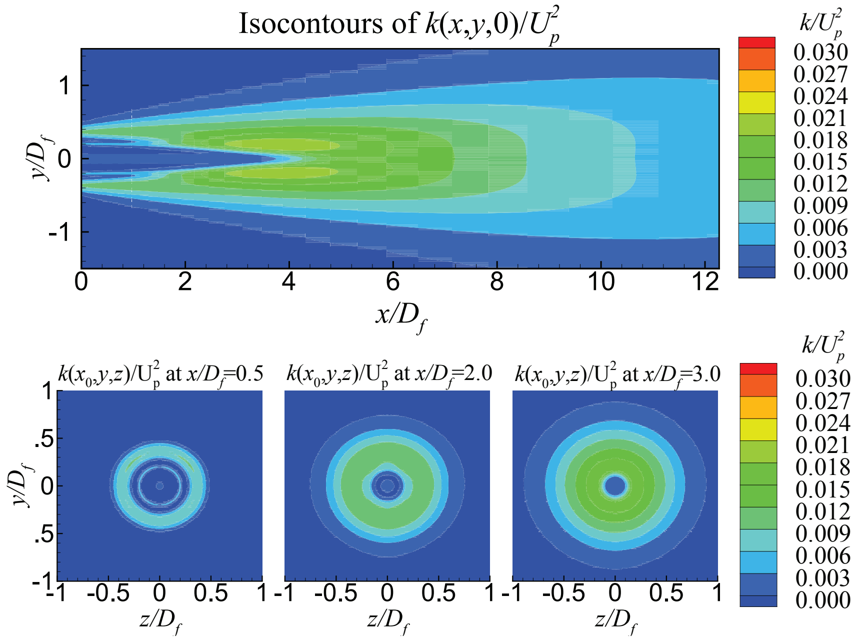

Figure 9. Computational TKE field for baseline nozzle at hot condition.

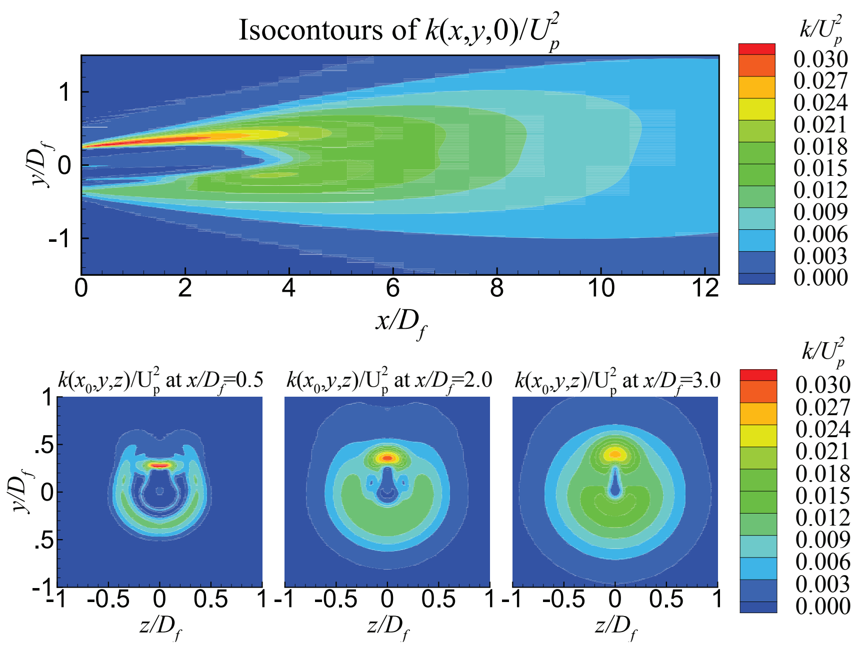

Figure 10. Computational TKE field for the solid wedge nozzle at hot condition.

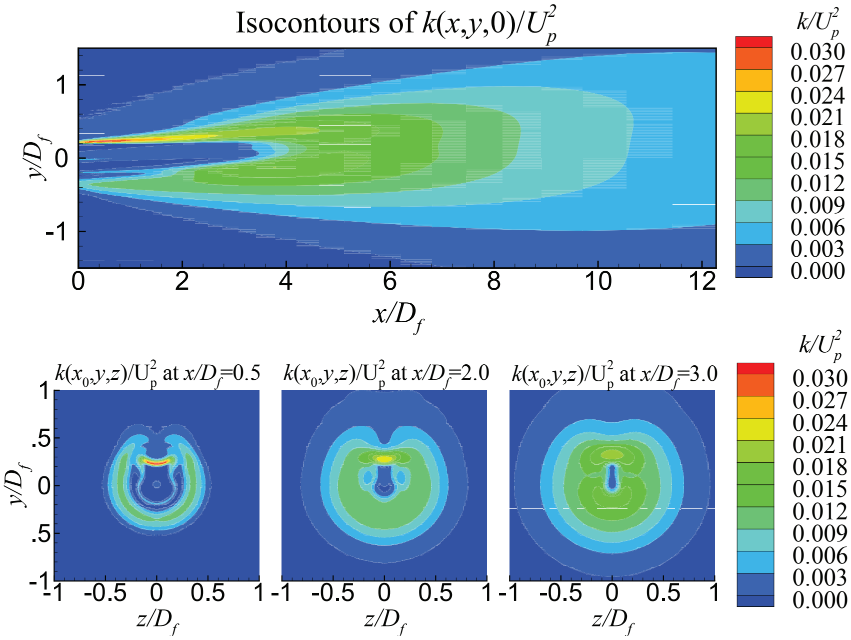

Figure 11. Computational TKE field for the solid flaps at($\beta = 1.0$) at hot condition.

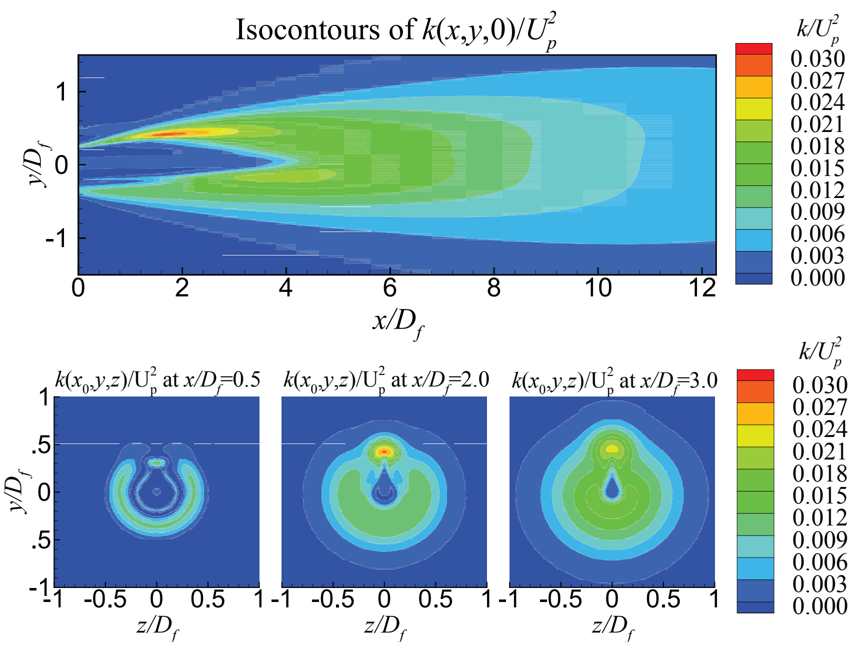

Figure 12. Computational TKE field for the porous flaps ($\beta = 0.5$) at hot condition.

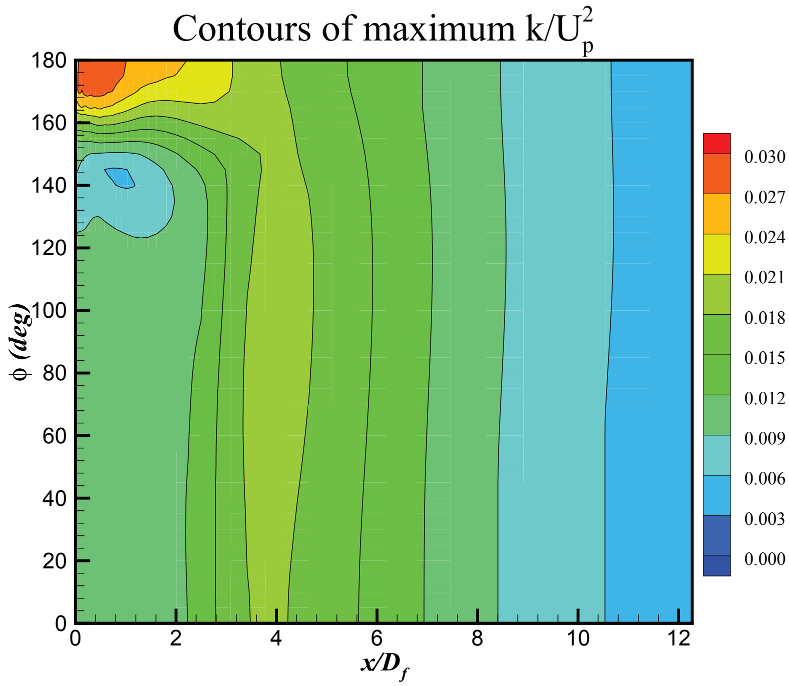

(a) Absolute

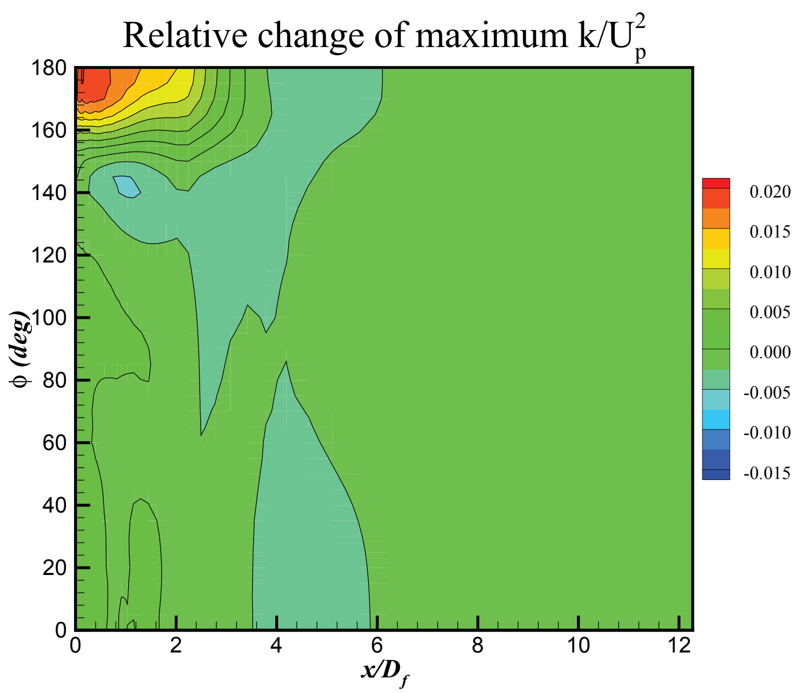

(b) Relative to baseline nozzle

Figure 13. Azimuthal variation of the peak turbulent kinetic energy for the porous flaps ($\beta = 0.5$).

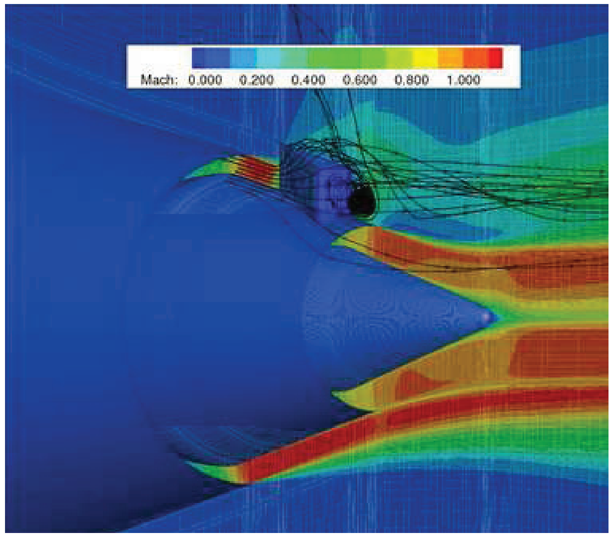

(a) Solid wedge

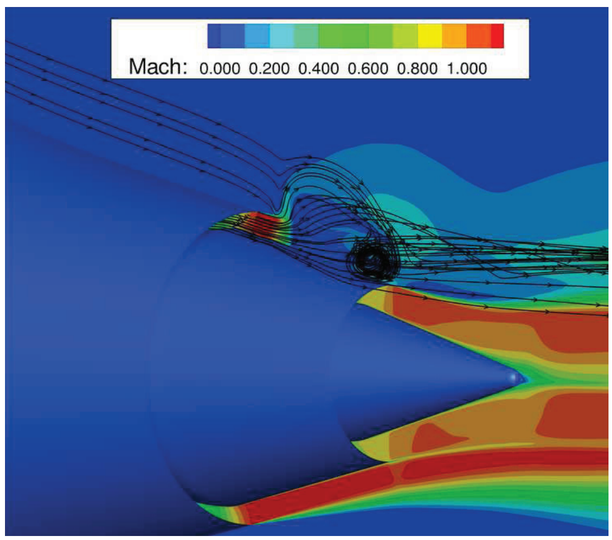

(b) Solid flaps ($\beta = 0.0$)

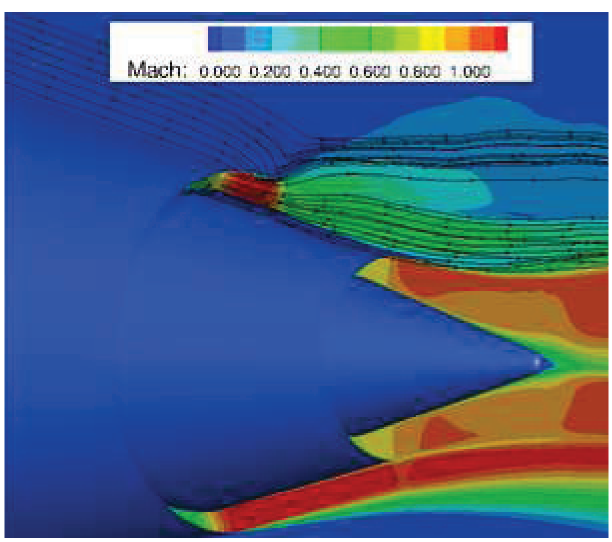

(c) Porous flaps ($\beta = 0.5$)

Figure 14. Mach number contour and streamlines around the deflectors.

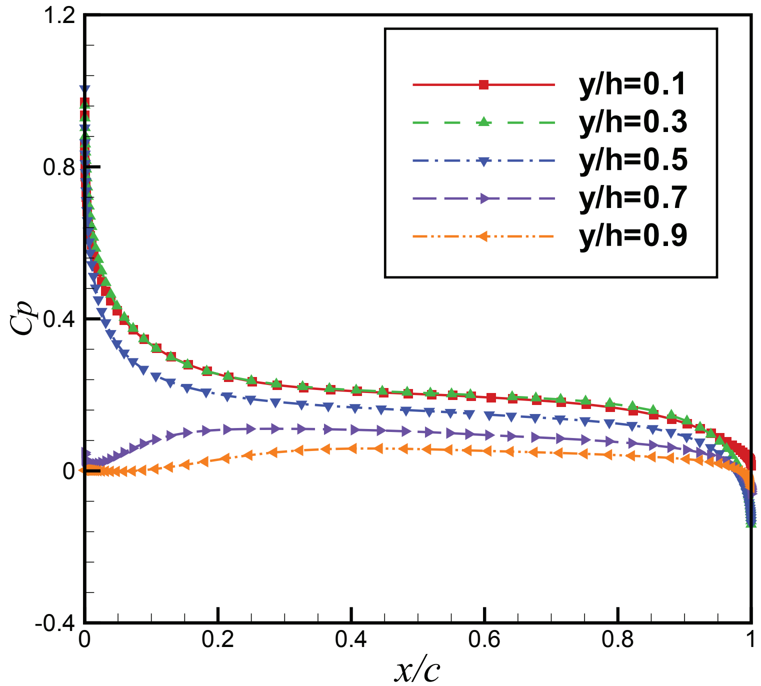

Figure 15. Pressure distribution along the surface of the solid wedge at different heights.

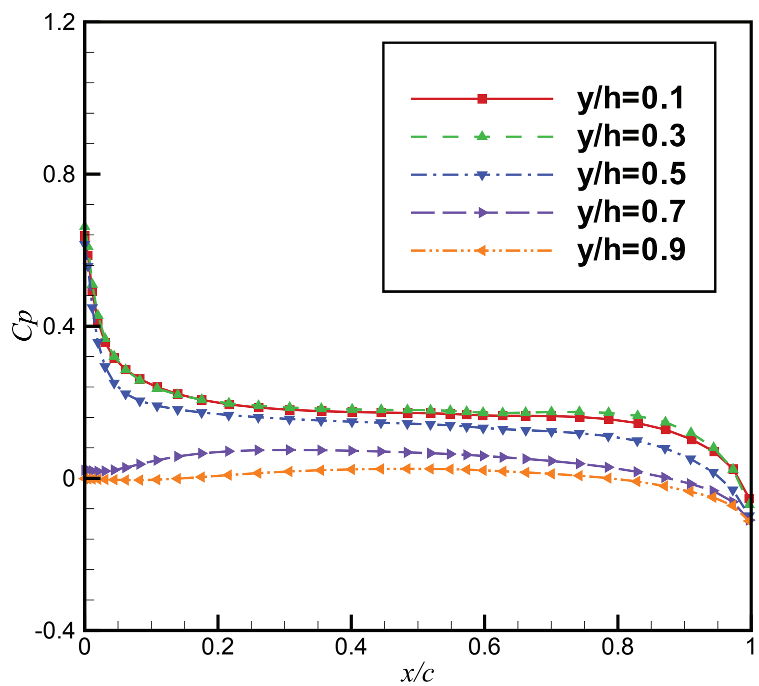

Figure 16. Pressure distribution along the surface of the porous flaps at different heights.